

Supporting Information

Triazoles: a new class of precursors for the synthesis of negatively charged carbon nitride derivatives

Dariya Dontsova^{†*}, Sergey Pronkin[‡], Marko Wehle^{††}, Zupeng Chen[†], Christian Fettkenhauer[†], Guylhaine Clavel[†], and Markus Antonietti[†]

[†] Max Planck Institute of Colloids and Interfaces, Department of Colloid Chemistry, Am Mühlenberg 1, 144476 Potsdam, Germany.

[‡] Institut de Chimie et des Procédés pour l'Energie, l'Environnement et la Santé (ICPEES), ECPM, CNRS-Université de Strasbourg (UdS) UMR 7515, 25, rue Becquerel, 67087 Strasbourg, France.

^{††} Max Planck Institute of Colloids and Interfaces, Theory & Bio-Systems Department, Am Mühlenberg 1, 14476 Potsdam, Germany.

Experimental Section.

Chemicals and Materials. Lithium chloride (99 %), potassium chloride (99 %), Rhodamine B (95 %) and hexachloroplatinic acid (H_2PtCl_6 , 8 wt. % aqueous solution) were purchased from Sigma Aldrich. 3,5-Diamino-1,2,4-triazole (98 %), 3-amino-1,2,4-triazole-5-thiol (98 %) and triethanolamine (TEOA, 98 %) were purchased from Alfa Aesar and dicyandiamide (DCDA, 98 %) from Merck. All the chemicals were used without further purification.

Synthesis procedures. *Bulk products* were prepared by heating a corresponding precursor with the ramp of 2.3 °C/min up to 550 °C and subsequent holding at this temperature for 4 h under constant nitrogen flow (15 mL/min) in a covered crucible. After cooling, products were thoroughly grinded.

Salt melt synthesis. Salts and a corresponding precursor(s) were ground together in a glove-box (mBraun Unilab, $\text{O}_2 < 0.1$ ppm, $\text{H}_2\text{O} < 0.1$ ppm) under argon atmosphere. Typically, the ratio between precursors and salts was 1 to 5 by weight, and relative quantities of salts corresponded to their eutectic composition. Reaction mixtures (~5-10 g) were transferred into porcelain crucibles and covered with lids. Crucibles were placed in the oven and heated under constant nitrogen flow (15 L/min) and atmospheric pressure at 550 °C for 4 hours with the ramp of 2.3 °/min. The crude products were removed from the crucibles, washed with deionized water (500 mL) for 15 hours in order to remove salts, then filtered,

extensively washed with DI water and dried in a vacuum oven (20 mbar) at 50 °C for 15 h. Reference mpg-CN was prepared according to the described procedure¹.

Photocatalytic tests.

Rhodamine B (RhB) photodegradation. 5 mg of a photocatalyst were dispersed in 5 mL of RhB solution in deionized water (10 mg/L). The suspension was agitated in dark for 30 minutes in order to reach dark-adsorption equilibrium, then illuminated with a blue LED module emitting at 465 nm (30 W, OSA Opto Lights) from a fixed distance of 5 cm. The RhB degradation was monitored as the decrease of the dye concentration over irradiation time. At specific time intervals (t), 300 μ L aliquots of the reaction mixture were taken, diluted with 1.7 mL of deionized water, kept for 30 minutes in a dark to allow catalyst precipitation, and then analyzed spectrophotometrically (T70 UV/VIS spectrophotometer of PG instruments Ltd.). Reaction rate constants k were calculated as the slopes of the linear fits of $[-\ln(A/A_0)]$ dependence on irradiation time. Here, A_0 and A are the measured at 550 nm absorbance of the dye in the solution after dark equilibration and after irradiation time t , respectively, which are proportional to the dye concentrations in the solution (C_0 and C).

Hydrogen evolution reactions (HER). HER were performed using a side-irradiated closed steel reactor equipped with a Teflon inlet, thermocouple, pressure sensor, magnetic stirring and thermostat, and connected to a Schlenk line. In all the cases, Pt and triethanolamine (TEOA) were used as a co-catalyst for H₂ generation and as a sacrificial hole-scavenger, respectively. Being a good buffering agent, TEOA provides stable pH of 10.8 for the whole duration of the experiment. The detailed description of the set-up and the test procedure can be found in literature² and below. Pt⁰ was in-situ photo-deposited onto tested photocatalysts using hexachloroplatinic acid (H₂PtCl₆) as a precursor. During the experiment, the buildup of pressure was monitored as a function of the irradiation time. 50 W white LED array was used as an irradiation source.

Hydrogen evolution set up and measurement procedure. All catalytic experiments were carried out under argon atmosphere. The double walled and thermostatically controlled reaction vessel was connected to a digital pressure sensor (Type-P30, DP =_0.1%, WIKA Alexander Wiegand SE & Co. KG, Germany) to monitor the pressure increase due to hydrogen evolution. 25 mg of sample were placed inside the reactor. Then the reactor was evacuated and refilled with argon for several times. H₂O and TEOA were pre-treated before use. H₂O was degassed first for 1 h under vacuum in an ultrasonic bath and followed by purging with argon for 1 h. TEOA was separately purged for 1 h with argon. The solvent mixture (38 mL), composed of water and triethanolamine (TEOA) in the ratio of 9/1 (v/v) and 19.7 μ L H₂PtCl₆ solution (corresponds to theoretical 3 wt. % of Pt loading onto the catalyst), were added, and the temperature was maintained at 25 °C by a thermostat. After

stirring for 10 min to reach thermal equilibrium, the reaction was started by switching on 50 W white LED array (Bridgelux BXRA-50C5300, $\lambda > 410$ nm). The amount of evolved gas was continuously monitored by means of the time dependent pressure increase. The hydrogen evolution rate was calculated according to the Ideal Gas law:

$$\dot{n} = \frac{n}{t} = 10^5 \frac{\Delta p \cdot V}{R \cdot T \cdot t}$$

where \dot{n} is hydrogen evolution rate [$\mu\text{mol/h}$], n moles hydrogen [μmol], t illumination time [h], Δp pressure increase [bar] during irradiation time t , V volume headspace above reaction solution, R universal gas constant [8.314 J/mol*K] and T temperature [298 K].

To confirm that the evolved gas is hydrogen, the headspace of the reactor was analyzed by mass spectrometry (Pfeiffer Vacuum ThermoStar GSD 301 T gas analyzing system; using argon as carrier gas) after the test.

Characterization. Powder X-Ray diffraction patterns were measured on a Bruker D8 Advance diffractometer equipped with a scintillation counter detector with $\text{CuK}\alpha$ radiation ($\lambda = 0.15184$ nm) applying 2θ step size of 0.05° and counting time of 3s per step. FT-IR spectra were recorded on a Varian1000 FT-IR spectrometer equipped with an attenuated total reflection unit applying a resolution of 4 cm^{-1} . Nitrogen adsorption/desorption measurements were performed after degassing the samples at 150°C for 20 hours using a Quantachrome Quadrasorb SI-MP porosimeter at 77.4 K. The specific surface areas were calculated by applying the Brunauer-Emmett-Teller (BET) model to adsorption isotherms for $0.05 < p/p_0 < 0.3$ using the QuadraWin 5.05 software package. Elemental analysis (EA) was accomplished as combustion analysis using a Vario Micro device. Scanning electron microscopy (SEM) images were obtained on a LEO 1550-Gemini microscope. Transmission electron microscopy (TEM) was performed on a CM200FEG (Philips) microscope, operated at 200 kV. Samples were prepared by depositing a drop of a suspension of particles in chloroform onto the amorphous carbon film. Thermogravimetric analysis (TGA) was carried out using a NETZSCH TG 209 F1. The samples were heated in aluminium oxide crucibles at a heating rate of 10 K min^{-1} under nitrogen gas flow. Optical absorbance spectra of powders were measured on a Shimadzu UV 2600 equipped with an integrating sphere. The absorption spectra of RhB solutions were recorded on a T70 UV/VIS spectrophotometer (PG instruments Ltd.). The emission spectra were recorded on LS-50B, Perkin Elmer instrument. The excitation wavelength was 350 nm. EDX investigations were conducted on a Link ISIS-300 system (Oxford Microanalysis Group) equipped with a Si(Li) detector and an energy resolution of 133 eV. The solid-state NMR $^{13}\text{C}\{^1\text{H}\}$ CP/MAS (cross-polarization magic angle spinning) measurement was carried out using a Bruker Avance 400 spectrometer operating at 100.6 MHz using a Bruker 4 mm double resonance probe-head operating at a spinning rate of 10 kHz. ^1H composite pulse decoupling was applied

during the acquisition. ^{13}C chemical shifts were referenced externally to TMS (tetramethylsilane) using adamantane as a secondary reference. X-ray photoelectron spectroscopy (XPS) was performed on a Multilab 2000 (Thermo) spectrometer equipped with Al $K\alpha$ anode ($h\nu = 1486.6$ eV). All spectra were referenced to the C 1s peak of adventitious carbon at 285.0 eV. For quantification purposes, survey spectra at pass energy of 50 eV and high-resolution spectra at pass energy of 20eV were recorded and analyzed by XPS Peak 4.1 software (written by Raymund Kwok). The spectra were decomposed assuming line shapes as sum functions of Gaussian (80 %) and Lorentzian (20 %) functions. Raw areas determined after subtraction of a Shirley background³ were corrected according to following sensitivity factors⁴ (C 1s: 0.25; N 1s: 0.42; O 1s: 0.66; K 2p: 1.24). ICP-AES measurements were performed on Perkin Elmer ICP OES 8000.

Mott-Schottky analysis was performed by measuring impedance spectra of the samples in a potential range from 0,40 to -0,60 V RHE, -0,02 V potential step, and frequencies from 10 kHz to 0,1 Hz, 7 mV potential amplitude. The measurements were performed in a standard three-compartment electrochemical cell. Pt coil and mercury sulfate electrodes were utilized as counter and reference electrodes correspondingly. The curves are presented in reversible hydrogen electrode scale RHE. (0,000 V RHE = -0,635 V Ag/AgCl for pH=7,0). The measurements were performed in 0,1 M phosphate buffer solution with pH=7,0. The solution was purged by N_2 before the measurements to remove oxygen; constant flow of N_2 was kept during the measurements in order to avoid oxygen leaking into the cell.

The electrodes were prepared by deposition of known amount of the powder on an Au substrate. Au was chosen as a substrate electrode due to 1) its low interfacial capacity comparing to other typical substrates, such as carbon or metal oxides (ITO, FTO), 2) high surface roughness and 3) positive surface charge helping to improve the adhesion of powder samples, whose surface is negatively-charged. In order to prepare the electrode the known amount of powder was ultrasonically dispersed in ethanol in order to make 100 mg/ml ink. Then 100 μl of ink was deposited on the Au substrate in 5 steps with drying in air between the steps. Finally, 40 μl of 5% solution of Nafion in ethanol was pipetted on the deposit to avoid its detachment. Preliminary experiments with pure Au substrate and Au+Nafion electrode were performed to demonstrate their negligible contribution into the measured capacity of electrodes with deposited samples powder.

Measured impedance spectra were fitted with the simplest equivalent circuit capable to fit experimental data: $R_1(CR_2)$. Here R_1 is related to the resistance of the electrolyte, R_2 is charge transfer resistance due to reduction of residual oxygen and/or evolution of hydrogen (close and below 0,00 V RHE), C is an interfacial capacity predominantly determined by space charge layer in the semiconducting electrode⁵. In order to take into account frequency dispersion of C due to surface inhomogeneity, the capacity was modelled as constant phase element Q ($-Z''=1/C(j\omega)^\alpha$) with fixed phase shift constant $\alpha=0,90$.

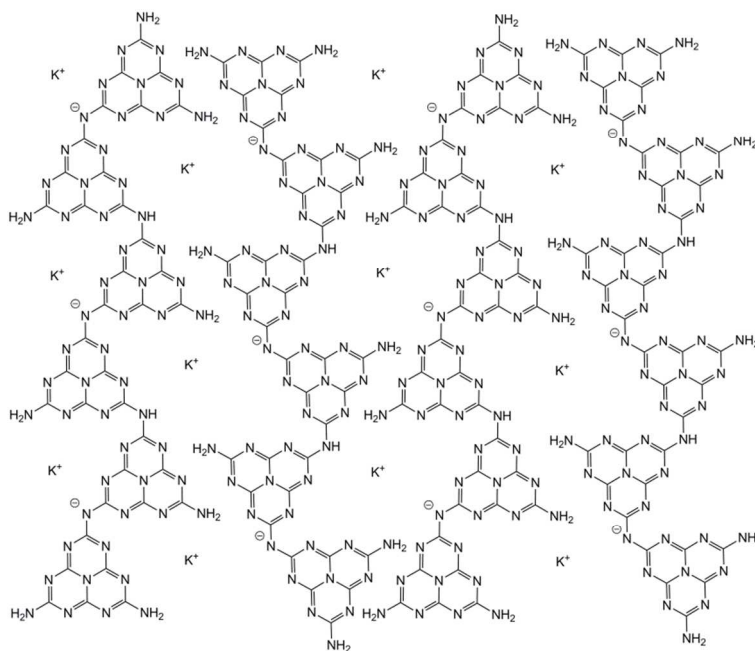
Computational details

Density Functional Theory (DFT) was chosen to compute fragments of the polymer to provide evidence for the materials' structure. Therefore molecular optimizations and computations were carried out using the Gaussian03⁶ software package and all conducted DFT calculations used the B3LYP theory level with the 3-21 basis set of functions^{7, 8}. Additionally, control quantum mechanics optimizations were also carried out on the Hartree-Fock (HF) theory level with the 3-21 basis set of functions⁹.

Systematic optimization and stability studies on different sizes of the Polymer-Fragments-Systems were performed to ascertain the critical fragmentation size in order to minimize side-effects of non-periodic systems, for the sake of computational efficiency. Varying the fragmented systems by sizes (2x2, 3x1.5 and 4x3 systems were attempted; here, the first number indicates the number of strands, and the second one corresponds to the number of repeating polymer units), we found that the critical minimal system size for our setup is 4x3, the other systems therefore will not be discussed in this experimental work. All atoms of the optimized and computed molecular systems were free to move, no computational restraints are given.

Structural models

The initial structural model was selected as explained below. Firstly, the repeating unit is shown in Figure 6d with the input $x=y=1$, which was derived from the XPS investigations and fits perfectly to the elemental composition of the LiCl/KCl-derived products. Next, considering the appearance of the HR-TEM images of the polymer (see Figure 7d) and H content that excludes a high condensation degree, the polymer structure was concluded to be based on 1D-melon strands of which the arrangement in the crystal structure was previously studied by B. Lotsch using semiempirical cluster calculations [ref. 26 in the manuscript]. According to Lotsch, "melon layers are made up from infinite chains of "melem-monomers" condensed via N(H)-bridges, thereby forming a closely packed two-dimensional array. The heptazine strands are arranged in a zig-zag-type fashion". The zig-zag-type arrangement suggested by Lotsch was maintained in our initial structural model, though the neighbouring melon strands had to be shifted (on y axis) and moved apart from each other (on x axis) to enable the accommodation of the quite large potassium ions in the resulting voids between the strands, according to the results of the PXRD investigations. The obtained structure clearly indicates that it is not possible to fit more K^+ ions in between the melon strands (i.e. it is not possible to obtain a polymer with $x=0$ in Figure 6d) maintaining their positions in between the strands. Thus, the resulting arrangement was used to perform single-layer studies. A (4 x 3) fragment (4 strands x 3 repeating units in each) according to the drawing below was selected as a model for an extended poly(heptazine imide) potassium salt (PHIK) sheet.



The initial structural model consisting of 4 strand of 3 repeating units of poly(heptazine imide) potassium salt used for optimization.

The construction of the initial 3D model was driven, first of all, by the conclusions from the PXRD studies, which indicate that the structure is layered with the distance of 0.3258 nm in between the layers; and that the melon strands and K^+ ions lines of one layer are positioned right above/under the melon strands and K^+ ions lines of the other layer, as visualized by HR-TEM studies (Figure 7d). Such positioning of layers is supported by its similarity with the crystal structure of a monomeric salt containing the same chemical elements and structural fragment as PHIK, namely anhydrous potassium melonate, $K_3C_6N_7(NCN)_3$ that was investigated by A. Sattler¹⁰. Sattler showed that in potassium melonate, melonate anions are positioned above/under each other and form a layered structure with a stacking distance of 0.328 nm. Following this, several different ways of positioning melon units towards each other were used. The following two options were considered for studies: 1) the second layer was an exact copy of the first layer, and 2) the second layer was obtained by the vertical rotation of the first layer at 180° and then fitting the melon strands and K^+ lines on top of each other (melon strands on top of melon strands; K^+ lines on top of K^+ lines). A $4 \times 3 \times 2$ (4 strands by 3 repeating units in each by 2 layers) fragment was used for optimization of the initial 3D structure.

Computational modeling results according to the Hartree–Fock method

In contrast to the B3LYP DFT calculation, the HF computations of the same model systems show stronger bending and distortion in the fragmented polymer strands and were carried

out only for comparison. Nonetheless, these HF optimized structures are in very close agreement with the measured results giving an average distance between the potassium ion line of 1.16 nm for the single-layer (Figure S9a) and 1.12 nm for the stacked 2-layer setup according to the model (1), without any rotation and translations in the input model. Additionally, the 2-layer model gave an average interlayer distance of 0.341 nm which is also in good agreement with the experimental and literature data (Figure S9b).

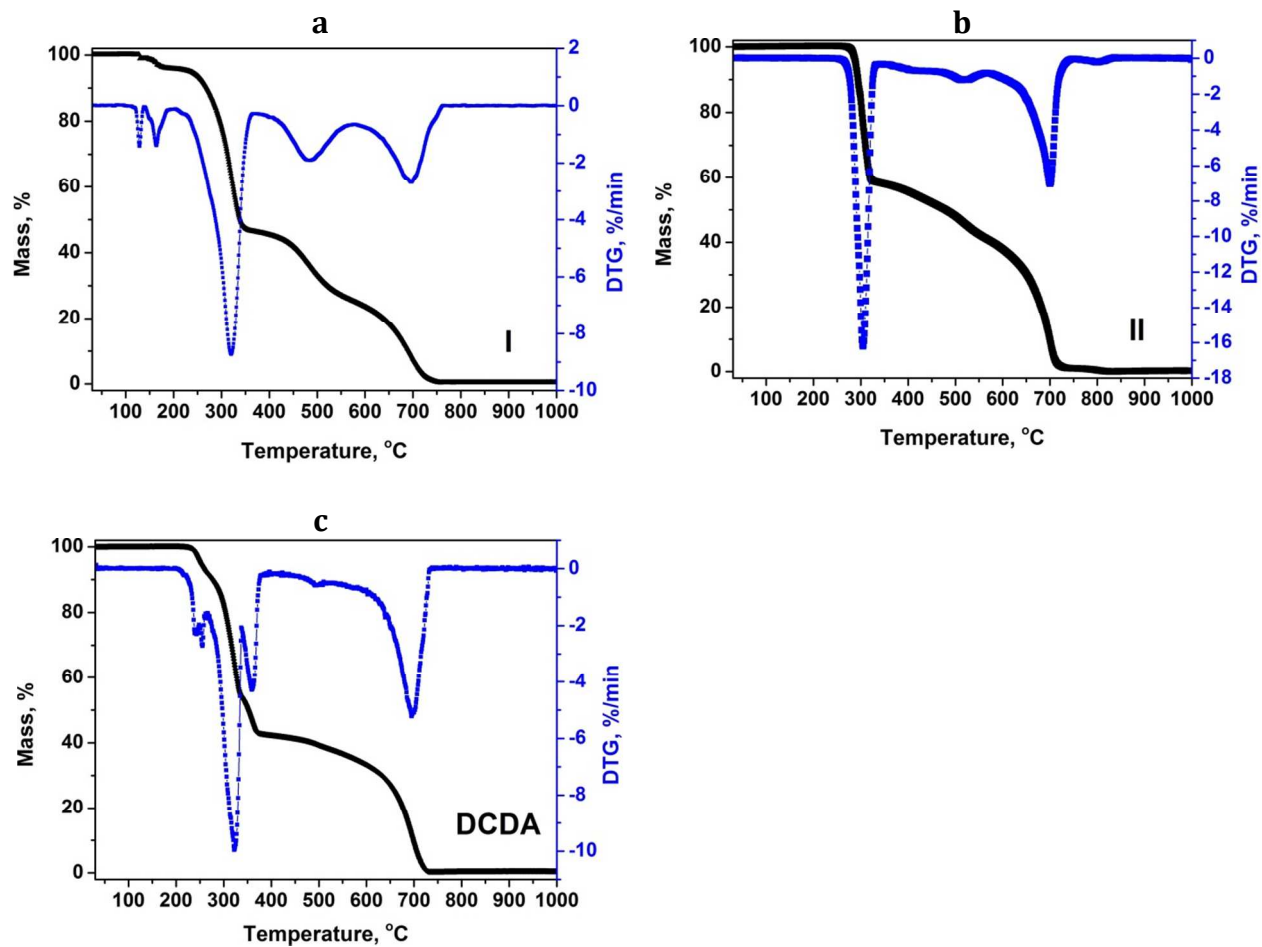
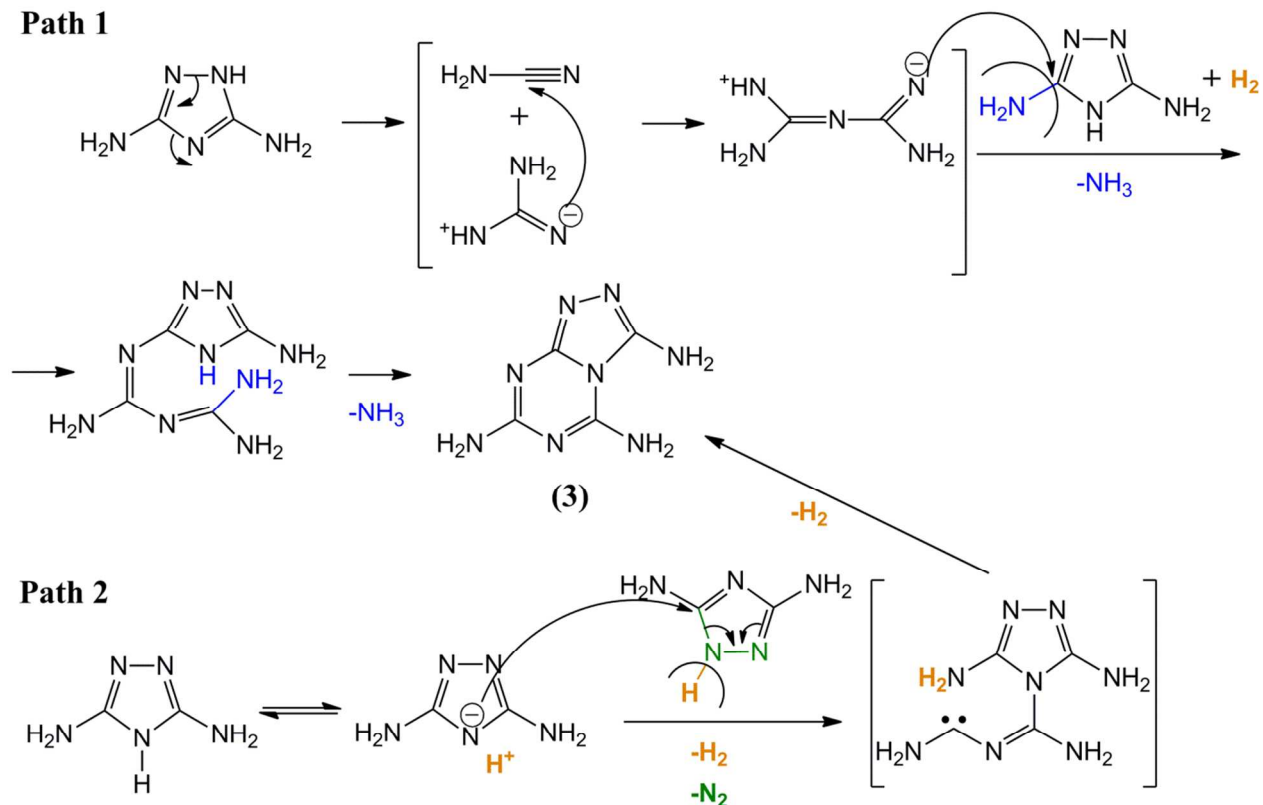
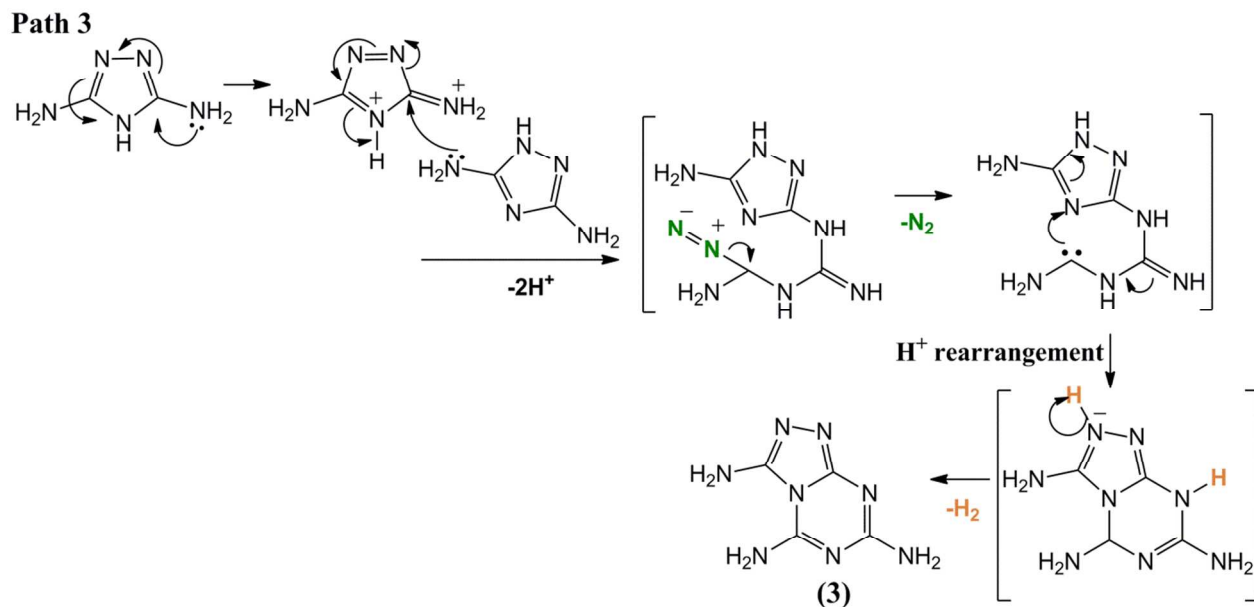


Figure S1. TGA (black) and DTG (blue) curves for guanazole (a), 3-amino-1,2,4-triazole-5-thiol (b) and dicyandiamide (c), a typical precursor for carbon nitride synthesis, for comparison.

Discussion of the possible reaction mechanism. We believe that guanazoguanazole (3) is most probably a reaction intermediate during conversion of 3,5-disubstituted 1,2,4-triazoles into poly(heptazine imides). (3) may be a reaction product of two molecules of guanazole as shown in Scheme S1, or originates from thermal decomposition of pyroguanazole (4)¹¹ which is a product of the trimerization of guanazole^{12,13}. If 3-amino-1,2,4-triazole-5-thiol is used as a precursor, the reaction mechanism differs only by the elimination of H₂S instead of NH₃.



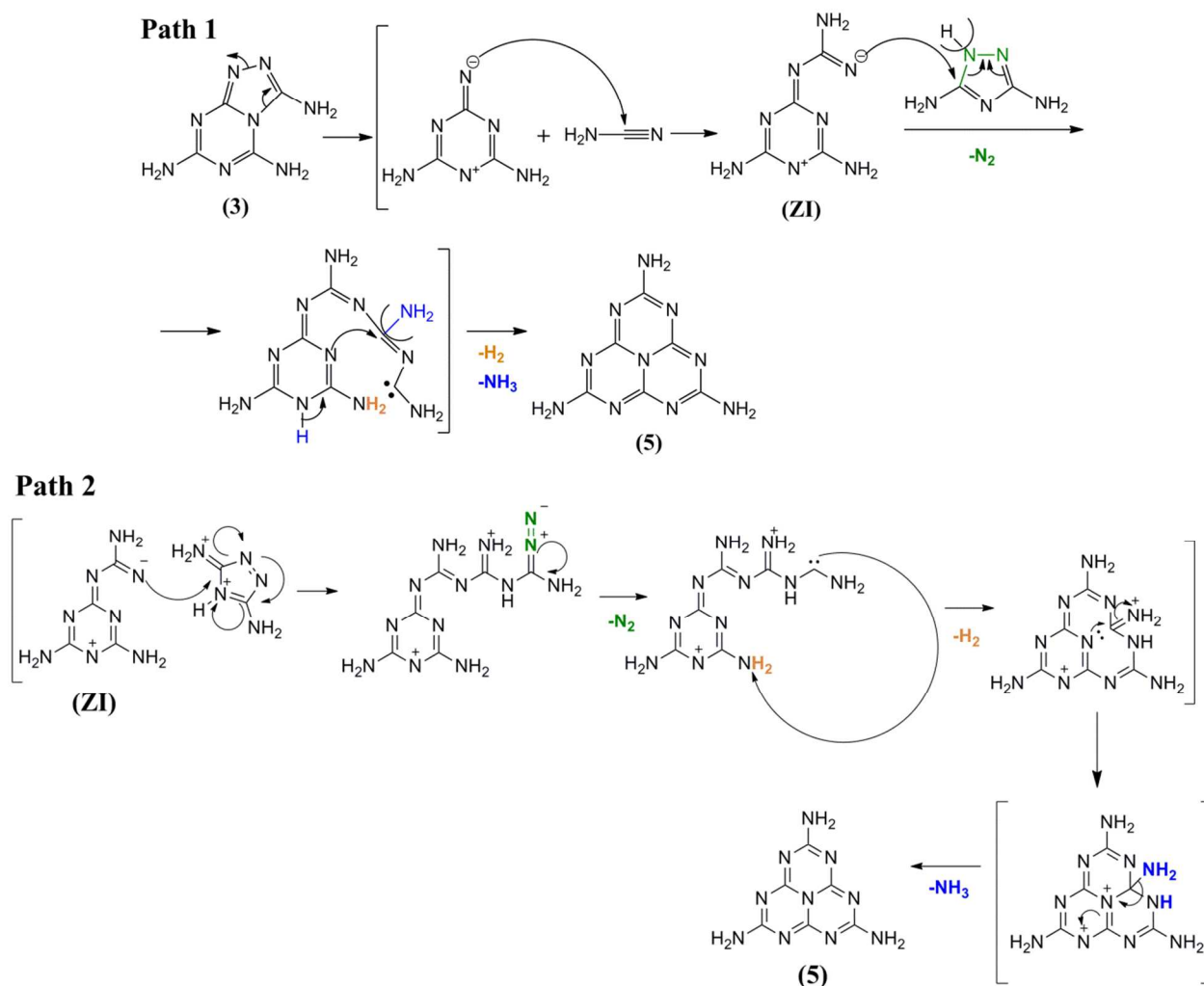


Scheme S1. Possible reaction mechanisms of guanazoguanazole (3) formation from guanazole.

In Scheme S1, the first reaction path of guanazole implies cleavage of the triazole ring at N1-N2 and C3-N4 positions, which is in agreement with computational studies of decomposition paths of substituted 1,2,4-triazoles¹⁴. Formed species may further react with the second molecule of guanazole and form (3) upon elimination of 2 ammonia molecules. However, this path requires 1 mole of H_2 . The second reaction path shown in Scheme 1 suggests a nucleophilic attack of the deprotonated guanazole on the C3 position of the second guanazole molecule, accompanied by elimination of N_2 and H_2 molecules, and formation of an intermediate carbene, which goes on to form (3) via the elimination of a H_2 molecule. The formation of Hydrogen according to the reaction path 2 can be used to realize path 1. For clarity it should be also noted that the position of the H-atom in the 1,2,4-triazole ring is not defined, especially at elevated temperatures¹⁵, and that in both precursors this H atom is acidic as discussed in the main text. Furthermore, at high temperatures both decomposition pathways of guanazole, namely by N1-N2 and C3-N4 bond cleavage and elimination of N_2 molecule, are possible due to sufficient energy supply. Alternatively (Path 3 in Scheme S1), the amino group attached to the 3/5 position of the triazole attacks into the ring to facilitate the $\text{N}=\text{N}$ bond production, the attack of another guanazole molecule pushes electrons round the ring in order to produce an azide species upon elimination of two protons. The presence of protic H atoms may facilitate the production of ammonia from the released N_2 atoms. The azide is then eliminated as N_2 producing a carbene intermediate which attacks the N4 of the second ring, pushing electrons through the next ring again onto the hydrogen of the ring which is eliminated as

hydride. This, combined with the release of a proton from the original ring, restores the aromaticity of the first ring yielding (3).

Guanazoguanazole (3) can undergo fragmentation on N1-N2 and C3-N4 bonds of the triazole ring, and rearrange forming a zwitterion ((ZI), Path 1, Scheme S2). This can further react with a molecule of guanazole, and produce a carbene upon elimination of an N₂ molecule, which stabilizes by elimination of ammonia and H₂ and forms melem (5) that is a known intermediate in the synthesis of the heptazine-based carbon nitride. Alternatively (Path 2, Scheme S2), the suggested zwitterion (ZI) attacks into a guanazole molecule producing an azide and, after release of N₂, carbene intermediate. This then attacks into the amino-group of the 6-membered ring, releasing hydrogen, then the central N atom attacks into the carbon atom featuring the C=NH₂⁺, and the subsequent release of ammonia quenches both the now-positive central N atom, and the N⁺ left from the zwitterion yielding melem (5).



Scheme S2. Possible reaction mechanisms of the guanazoguanazole (3) conversion into melem (5).

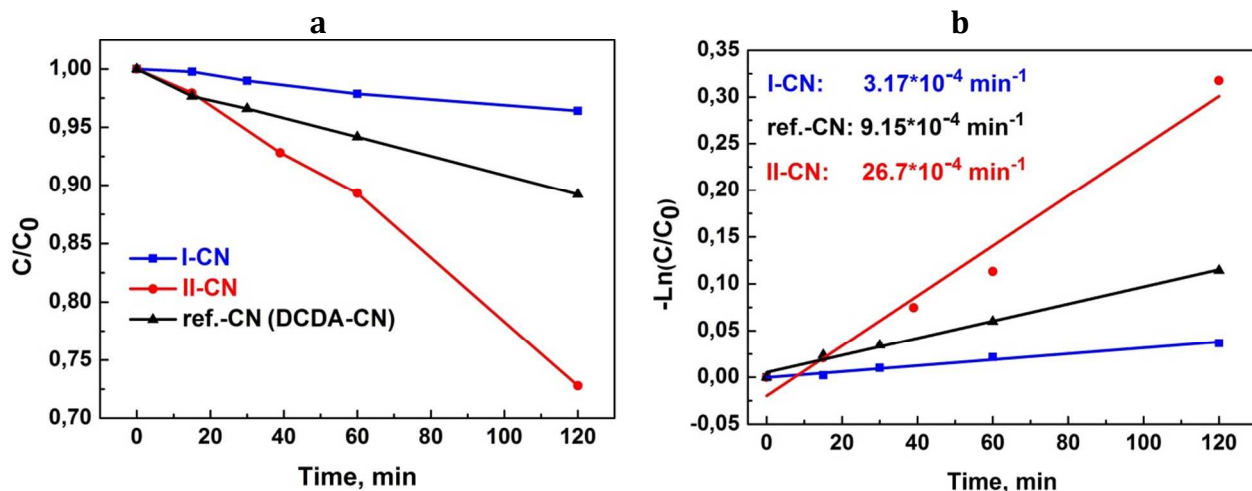


Figure S2. (a) Change of Rhodamine B relative concentration as a function of irradiation time, (b) dependence of $-\ln(C/C_0)$ on the reaction time.

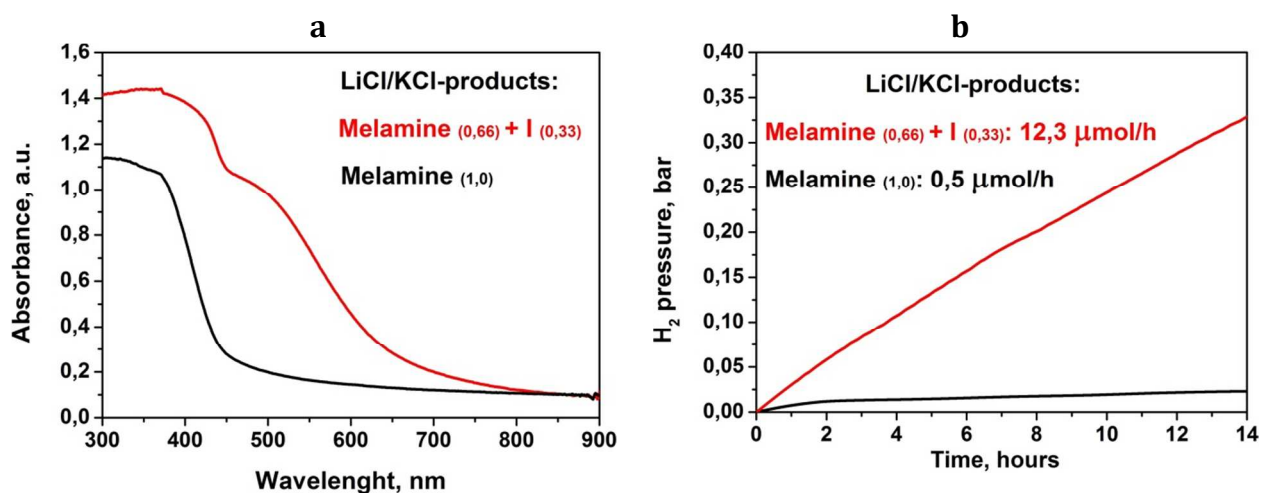


Figure S3. Improved visible light absorption (a) and, as a result, hydrogen evolution rate (b) achieved by using guanazole (I) as a co-monomer for preparation of CN-polymers in LiCl/KCl salt melt at 500 °C under N_2 . Amount of I used for co-condensation was a half of molar amount of melamine taken; and ratio of precursors to salts was 1 to 5 by weight.

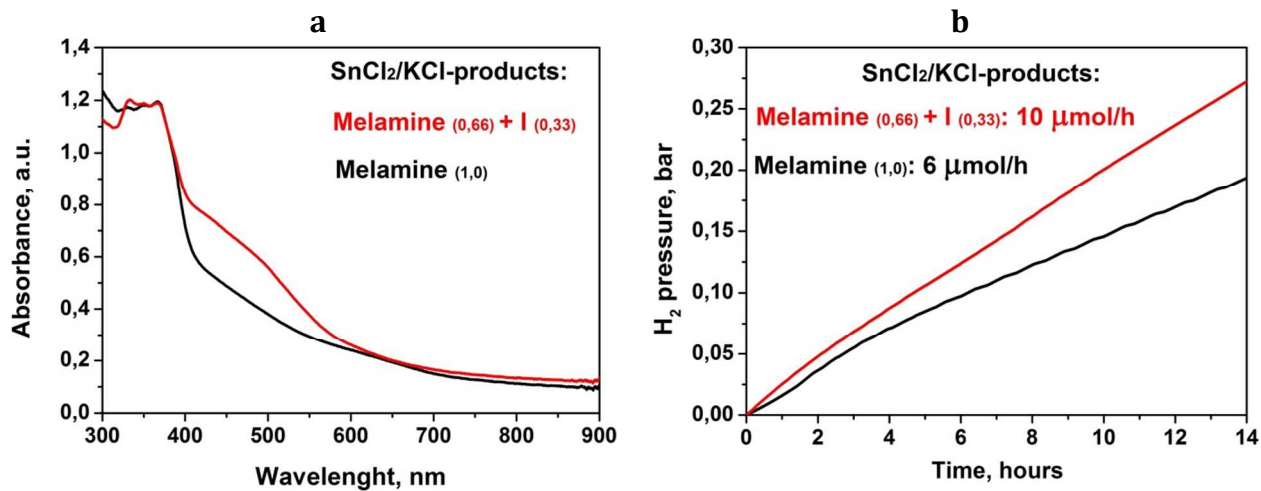


Figure S4. Improved visible light absorption (a) and, as a result, hydrogen evolution rate (b) achieved by using guanazole (I) as a co-monomer for preparation of CN-polymers in KCl/SnCl₂ salt melt at 550 °C under N₂. Amount of I used for co-condensation was a half of molar amount of melamine taken; and ratio of precursors to salts was 1 to 5 by weight.

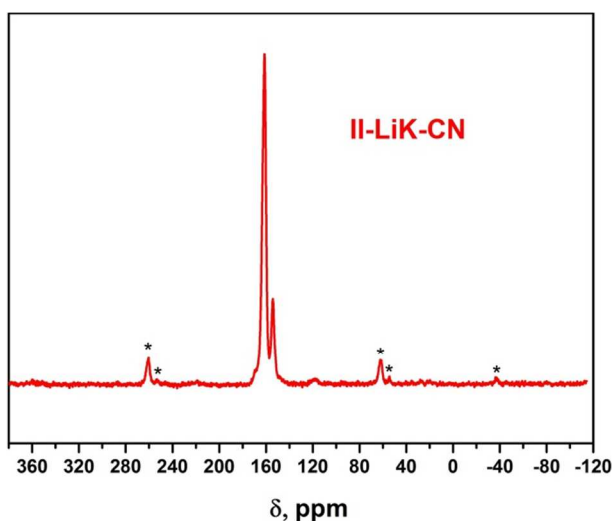


Figure S5. Solid state ¹³C{¹H} CP/MAS NMR spectra of carbon nitride synthesized from [2] in LiCl/KCl salt melt. Asterisks indicate spinning side bands in the ¹³C spectra.

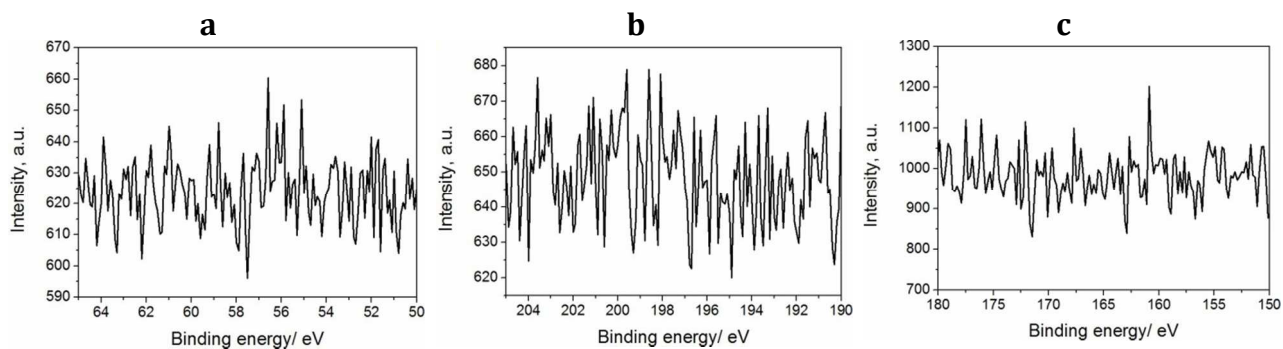


Figure S6. (a) Li1s, (b) Cl2p and (c) S2p XP spectra of II-LiK-CN.

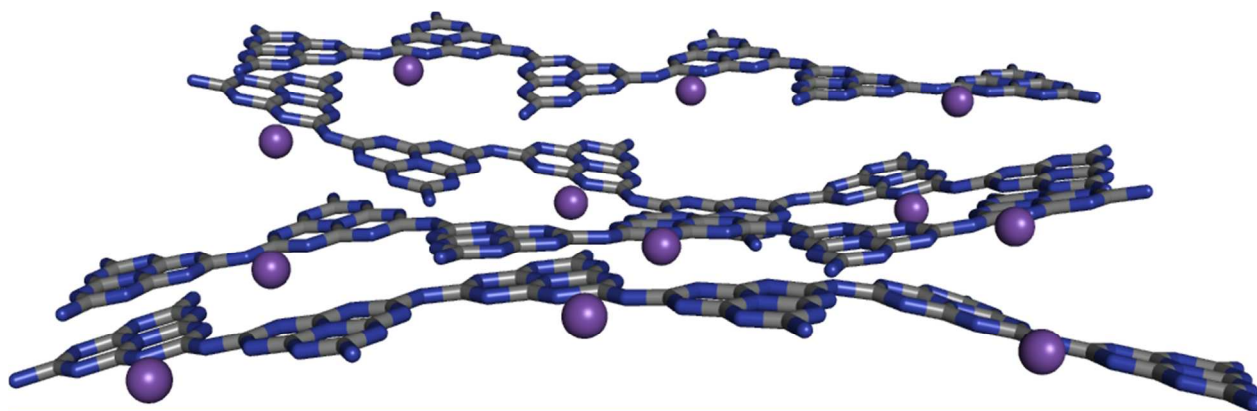


Figure S7. Side view of a B3LYP/3-21 DFT optimized 4x3 single layer system. Hydrogen atoms not shown, carbons in grey, nitrogen in blue, potassium ions as purple spheres.

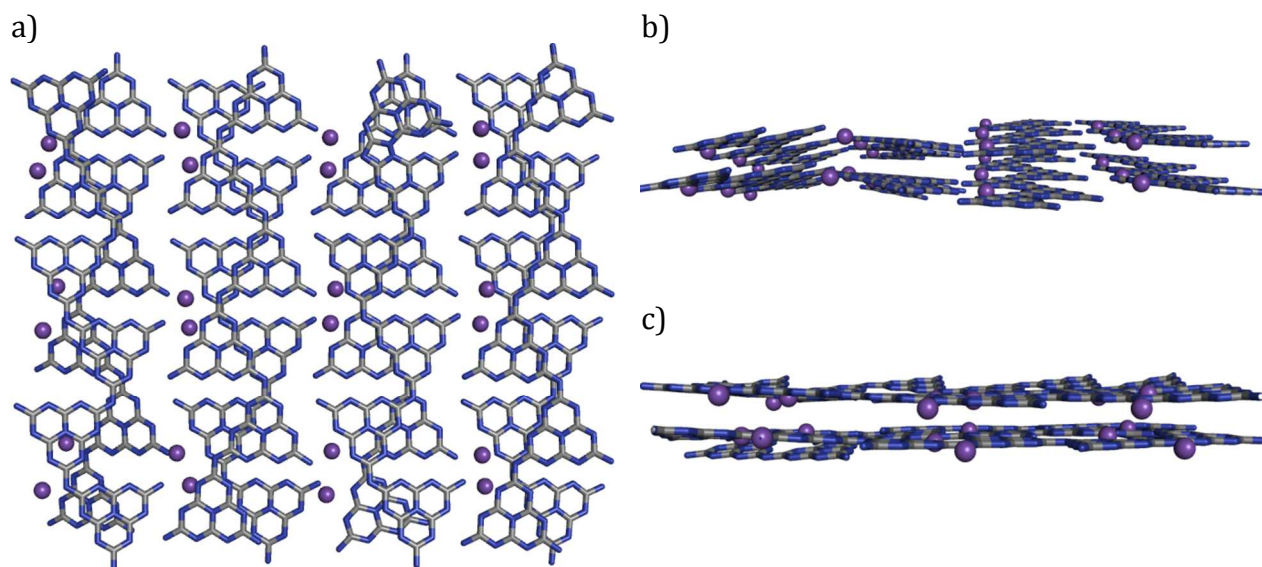


Figure S8. a) Top view of a B3LYP/3-21 DFT optimized 4x3x2 2-layer system according to the stacking model (2); side view of B3LYP/3-21 DFT optimized 4x3x2 2-layer systems according to a) the stacking model (1) and b) stacking model (2).

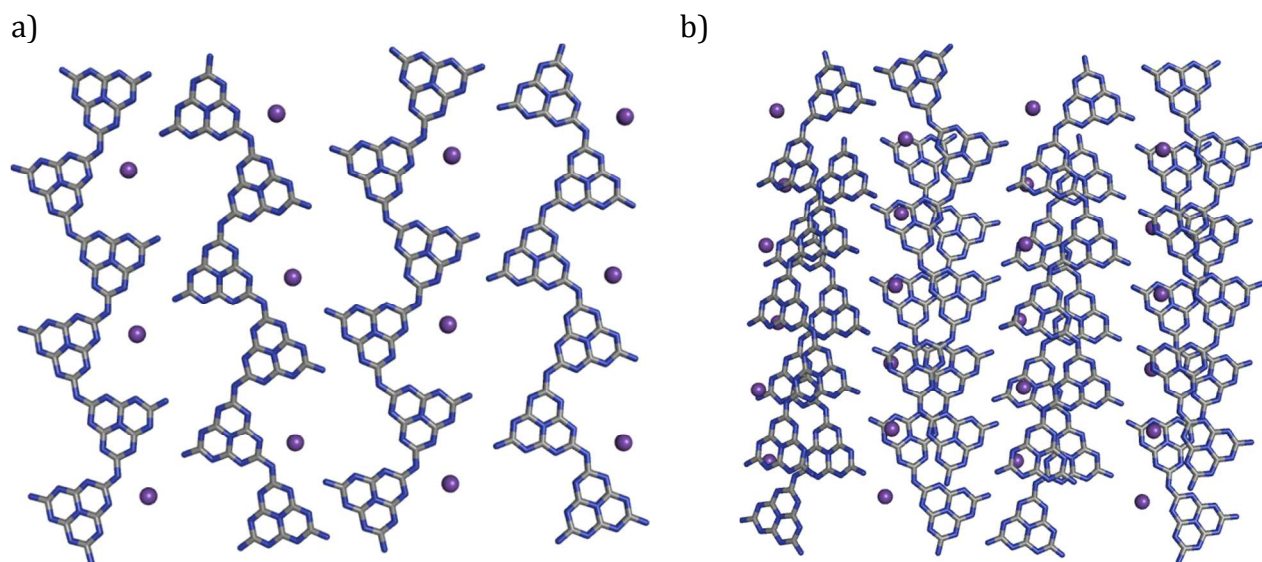


Figure S9. a) Top view of a HF/3-21 optimized 4x3 single layer system; b) Top view of a HF/3-21 optimized 4x3x2 2-layer systems according to the stacking model (1).

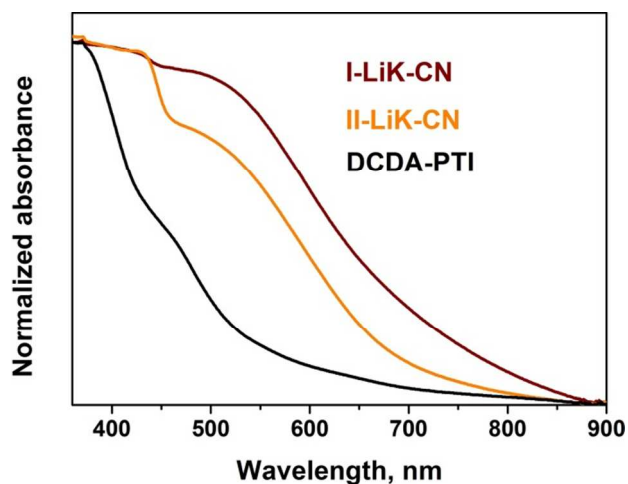


Figure S10. UV-Vis diffuse reflectance spectra of LiCl/KCl derived products.

Precursor/Melt (Weight Ratio)	T, °C	Yield, %	Color	BET s.a. m ² /g	H ₂ evolution rate, μmol/h
DCDA/LiCl-KCl (1:5)	550	20.5	yellow	43	0
II/LiCl-KCl (1:5)	450	50	orange	n/a	~0
II/LiCl-KCl (1:5)	500	36	orange	90	22.8
II/LiCl-KCl (1:5)	550	41	orange	31	20.3
II/LiCl-KCl (1:5)	600	17	yellow-orange	102	30.5
II/LiCl-KCl (1:2)	550	35	dark-yellow	31	25.5
II/LiBr-KBr (1:5)	550	59	yellow	37	14.2
II/LiCl-KCl (1:10)	550	23	red-brown	50	26.1
I/LiCl-KCl (1:5)	450	61	yellow-brown	40	n/a
I/LiCl-KCl (1:5)	500	44	red-brown	62	0.45
I/LiCl-KCl (1:5)	550	47	red-brown	40	3.3
I/LiCl-KCl (1:5)	600	12	red-brown	37	n/a

Table S1. Influence of the synthesis conditions such as synthesis temperature and reaction mixture composition on the activity of products in water reduction reaction. n/a – not analyzed.

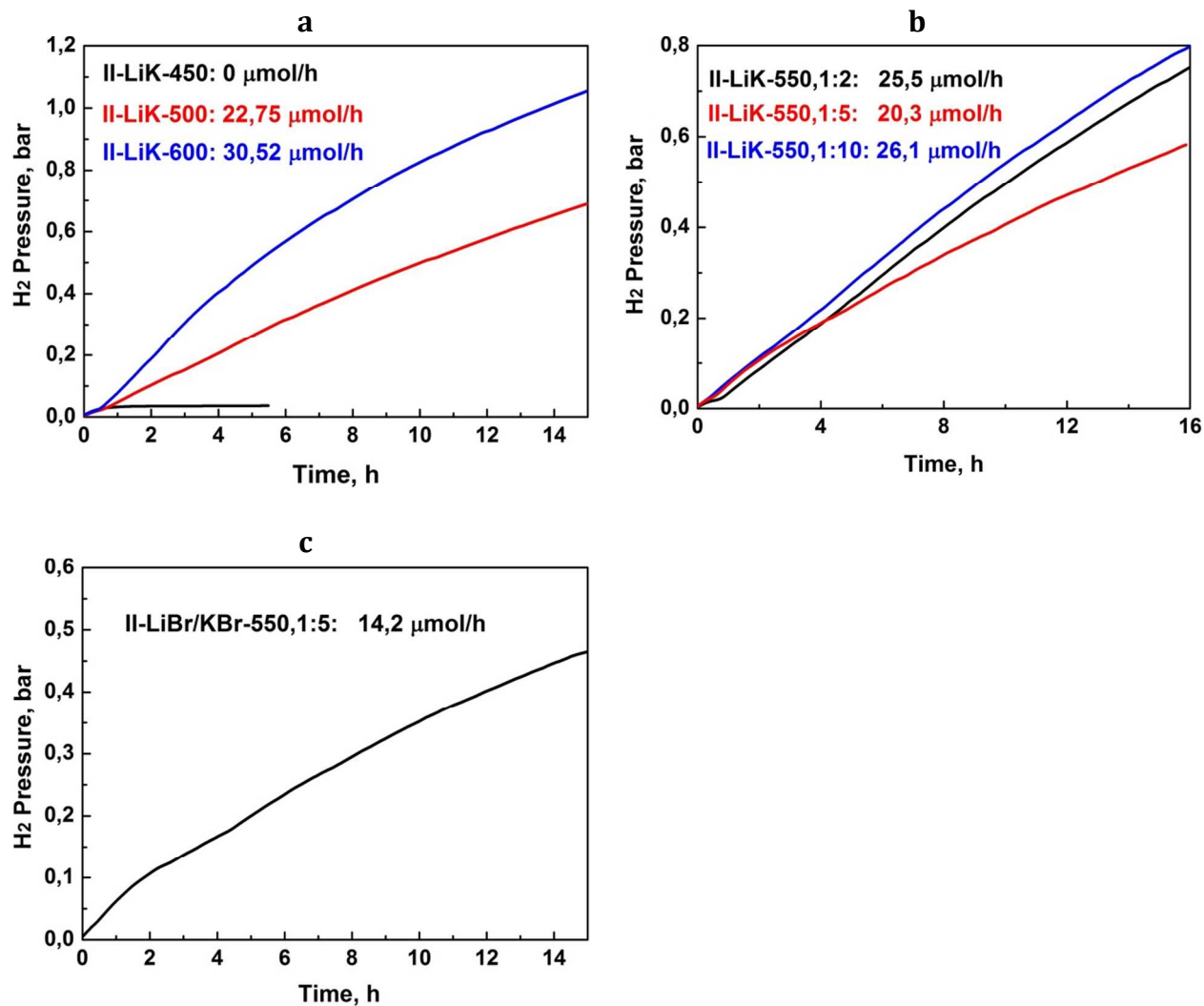


Figure S11. Photocatalytic hydrogen production using catalysts prepared from [2] in LiCl/KCl eutectic (a) at different temperatures, (b) at different precursor-to-salts weight ratios; (c) photocatalyst prepared at 550 °C in LiBr/KBr eutectic, at 1:5 precursor-to-salts weight ratio.

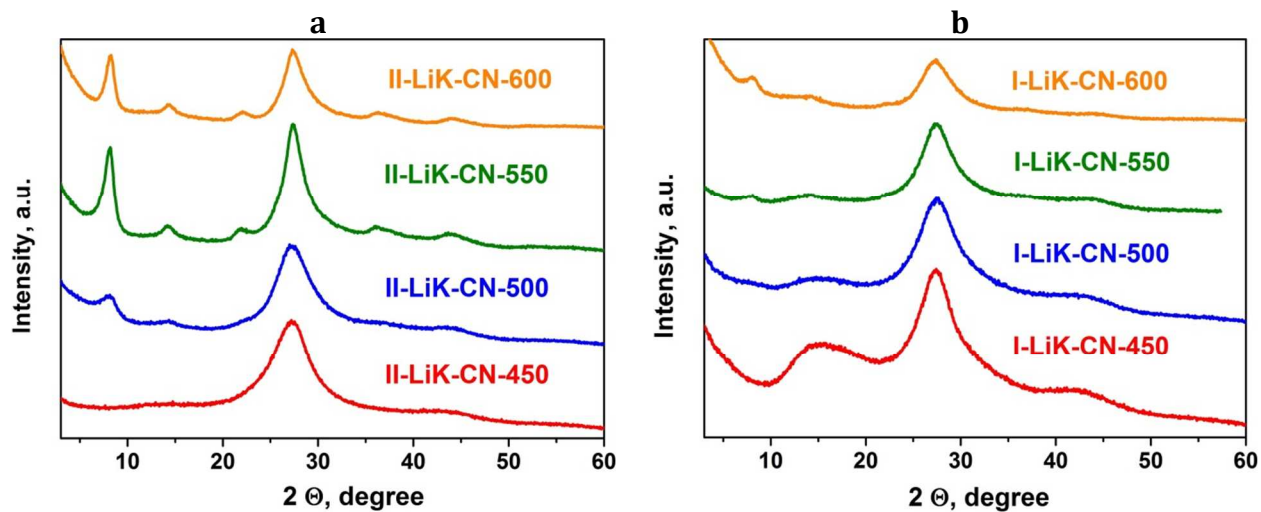


Figure S12. XRD patterns of products synthesized from (a) [2] and (b) [1] in LiCl/KCl salt melts at different temperatures.

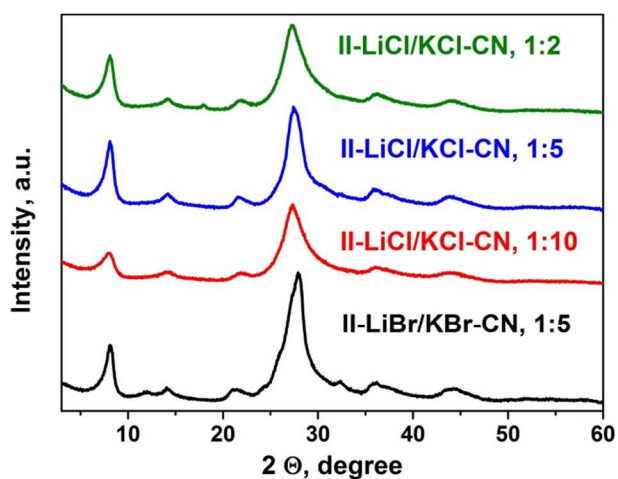


Figure S13. XRD patterns of products synthesized from [2] in LiCl/KCl and LiBr/KBr salt melts at different precursor to salts weight ratios.

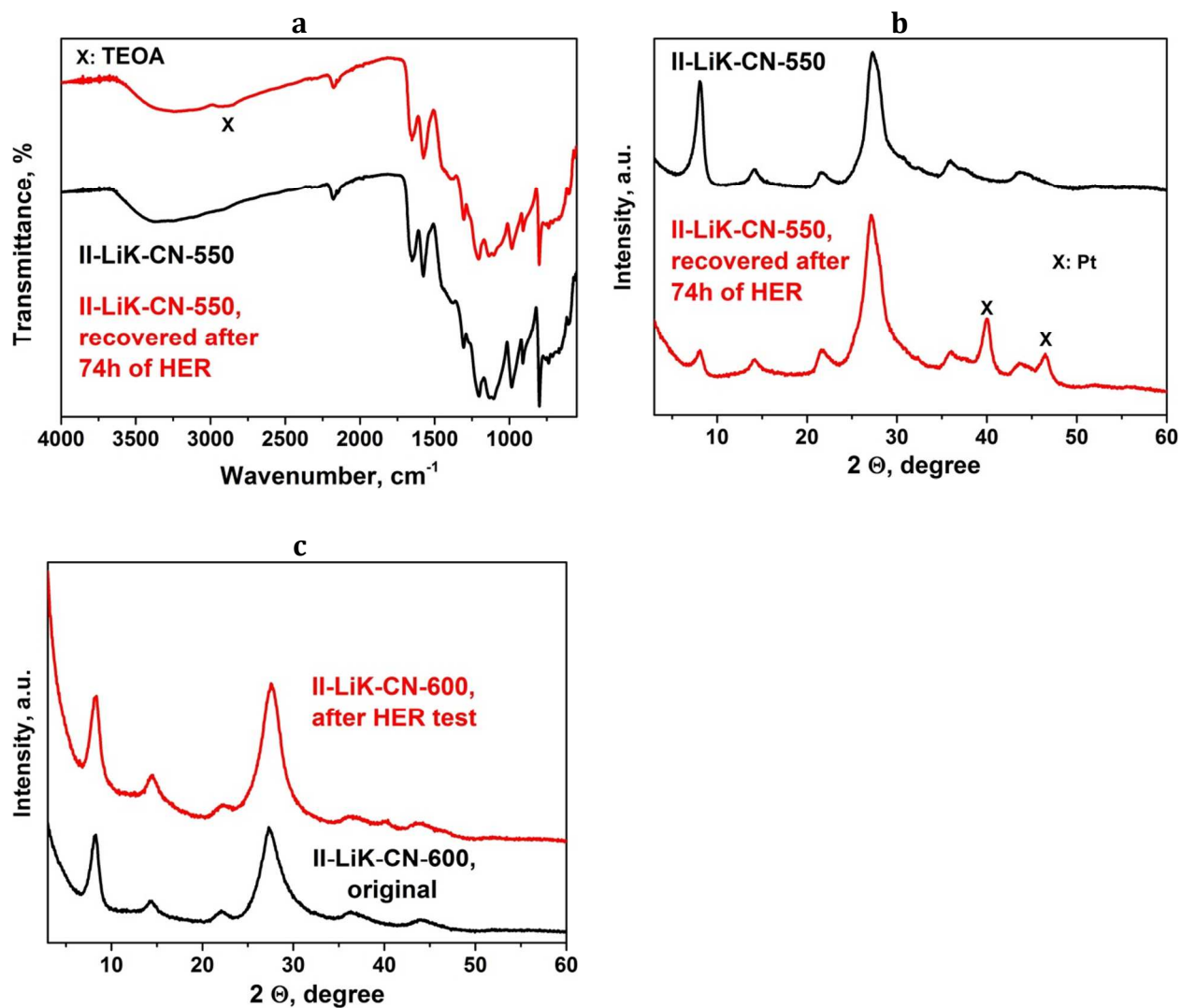


Figure S14. (a) FTIR-ATR spectra and (b) WAXS patterns of II-LiK-CN-550 before and after sustained (74 hours) hydrogen evolution. The intensity decrease of the reflection at $2\theta = 8^\circ$ is attributed to the loss of the smallest catalyst particles during isolation step, in which this reflection is more pronounced. (c) WAXS patterns of II-LiK-CN-600 before and after 22 hours of hydrogen evolution reaction.

II-LiK-CN-550	C, wt.%	N, wt.%	H, wt.%	O, wt.%	K, wt.%	Pt, wt.%
before HER	32.7	53.0	2.50	4.78	7.07	0
after HER	32.0	43.6	3.24	13.8	6.78	0.60

Table S2. Elemental composition of II-LiK-CN-550 (according to EDX; H content was analyzed by EA) before and after sustained (74 hours) hydrogen evolution. Increased content of C, O and H after the reaction is due to strong adsorption of triethanolamine at the surface of the catalyst as corroborated by FTIR spectrum (Figure S11a), where C-H stretching vibrations are observed.

- Groenewolt, M.; Antonietti, M., Synthesis of g-C₃N₄ Nanoparticles in Mesoporous Silica Host Matrices. *Adv. Mater.* **2005**, *17*, 1789-1792.
- Schwarze, M.; Stellmach, D.; Schroder, M.; Kailasam, K.; Reske, R.; Thomas, A.; Schomacker, R., Quantification of photocatalytic hydrogen evolution. *Phys. Chem. Chem. Phys.* **2013**, *15*, 3466-3472.
- Shirley, D. A., High-resolution X-ray photoemission spectrum of the valence bands of gold *Phys. Rev. B* **1972**, *5*, 4709-4714.
- Wagner, C. D.; Davis, L. E.; Zeller, M. V.; Taylor, J. A.; Raymond, R. H.; Gale, L. H., Empirical atomic sensitivity factors for quantitative analysis by electron spectroscopy for chemical analysis. *Surf. Interface Anal.* **1981**, *3*, 211-225.
- Rajeshwar, K., *Fundamentals of semiconductors electrochemistry and photoelectrochemistry*. VCH: 2007; Vol. 6.
- Gaussian 03, Revision C.02, Frisch, M.J., et al. G. W. Trucks, H. B. Schlegel, G. E. Scuseria, M. A. Robb, J. R. Cheeseman, J. A. Montgomery, Jr., T. Vreven, K. N. Kudin, J. C. Burant, J. M. Millam, S. S. Iyengar, J. Tomasi, V. Barone, B. Mennucci, M. Cossi, G. Scalmani, N. Rega, G. A. Petersson, H. Nakatsuji, M. Hada, M. Ehara, K. Toyota, R. Fukuda, J. Hasegawa, M. Ishida, T. Nakajima, Y. Honda, O. Kitao, H. Nakai, M. Klene, X. Li, J. E. Knox, H. P. Hratchian, J. B. Cross, C. Adamo, J. Jaramillo, R. Gomperts, R. E. Stratmann, O. Yazyev, A. J. Austin, R. Cammi, C. Pomelli, J. W. Ochterski, P. Y. Ayala, K. Morokuma, G. A. Voth, P. Salvador, J. J. Dannenberg, V. G. Zakrzewski, S. Dapprich, A. D. Daniels, M. C. Strain, O. Farkas, D. K. Malick, A. D. Rabuck, K. Raghavachari, J. B. Foresman, J. V. Ortiz, Q. Cui, A. G. Baboul, S. Clifford, J. Cioslowski, B. B. Stefanov, G. Liu, A. Liashenko, P. Piskorz, I. Komaromi, R. L. Martin, D. J. Fox, T. Keith, M. A. Al-Laham, C. Y. Peng, A. Nanayakkara, M. Challacombe, P. M. W. Gill, B. Johnson, W. Chen, M. W. Wong, C. Gonzalez, and J. A. Pople, Gaussian, Inc., Wallingford CT, 2004.
- Becke, A. D., Density-functional exchange-energy approximation with correct asymptotic behavior, *Phys. Rev. A* **1988**, *38*, 3098-3100.
- Lee, C; Weitao Yang, Parr, R. G., Development of the Colle-Salvetti correlation-energy formula into a functional of the electron density. *Phys. Rev. B* **1988**, *37*, 785-789.

9. Hartree, D. R., *The calculation of Atomic Structures*, **1957**, New York: Wiley & Sons.
10. Sattler, A., *Investigations into s-Heptazine-Based Carbon Nitride Precursors*, Ludwig-Maximilians-Universität München, **2010**, pp. 139-142.
11. Mosby, W. L., *The Chemistry of Heterocyclic Compounds, Part 2*, Vol. 15, Heterocyclic Systems with Bridgehead Nitrogen Atoms, Wiley **2007**.
12. Kaiser, D. W.; Peters, G. A.; Wystrach, V. P., Chemistry of Dicyandiamide. V. Structures of Guanazo- and Pyro-Guanazoles, and Reaction of Dicyandiamide with 3-Amino-5-Substituted-1, 2, 4, 4H-Triazoles. *J. Org. Chem.*, **1953**, *18*, 1610–1615.
13. Hofmann, K. A.; Ehrhart, O., *Berichte der deutschen chemischen Gesellschaft*, **1912**, *45* (2), 2731–2740.
14. Tagomori, S.; Kuwahara, Y.; Masamoto, H.; Shigematsu, M.; Kowhakul, W., *Int. Proc. Chem. Biol. Environ. Eng.* **2013**, *58*, 66-70.
15. Potts, K. T., The Chemistry of 1, 2, 4-Triazoles. *Chem. Rev.* **1961**, *61* (2), 87-127.